nature materials

LETTERS

PUBLISHED ONLINE: 24 JULY 2011 | DOI: 10.1038/NMAT3072

Bifurcation-based acoustic switching and rectification

N. Boechler†, G. Theocharis† and C. Daraio*

Switches and rectification devices are fundamental components used for controlling the flow of energy in numerous applications. Thermal[1–4] and acoustic[5–8] rectifiers have been proposed for use in biomedical ultrasound applications[6,7], thermal computers[2,9], energy- saving and -harvesting materials[5,6], and direction-dependent insulating materials[1–3]. In all these systems the transition between transmission states is smooth with increasing signal amplitudes. This limits their effectiveness as switching and logic devices, and reduces their sensitivity to external conditions as sensors. Here we overcome these limitations by demonstrating a new mechanism for tunable rectification that uses bifurcations and chaos. This mechanism has a sharp transition between states, which can lead to phononic switching and sensing. We present an experimental demonstration of this mechanism, applied in a mechanical energy rectifier operating at variable sonic frequencies. The rectifier is a granular crystal, composed of a statically compressed one-dimensional array of particles in contact, containing a light mass defect near a boundary. As a result of the defect, vibrations at selected frequencies cause bifurcations and a subsequent jump to quasiperiodic and chaotic states with broadband frequency content. We use this combination of frequency filtering and asymmetrically excited bifurcations to obtain rectification ratios greater than 10^4. We envisage this mechanism to enable the design of advanced photonic, thermal and acoustic materials and devices.

Periodicity in materials has proven useful for the control of wave propagation in electronic and photonic[10], mechanical[11], acoustic[12] and optomechanical[13] systems. The presence of nonlinearity in periodic dynamical systems makes available an array of useful phenomena (including localization, breathers, bifurcation and chaos)[14–19]. Here we study how the interplay of periodicity, nonlinearity, and asymmetry in granular crystals results in novel types of switching and rectification devices.

Granular crystals are densely packed arrays of elastic particles that interact nonlinearly through Hertzian contacts[20,21]. These systems are tunable from near-linear to strongly nonlinear dynamical regimes by changing the ratio of static to dynamic interparticle displacements[21,22]. Granular crystals have allowed the exploration of fundamental phenomena[5,21–28], and have been applied in engineering devices[29,30]. Here we study a granular crystal that is a statically compressed one-dimensional array of $N = 19$ stainless steel spherical particles (Fig. 1a,b). The particles are of measured radius $R = 9.53$ mm and mass $M = 28.84$ g, except for a single defect particle of radius $r = 5.56$ mm and mass $m = 5.73$ g placed at the second site from the left boundary. Longitudinal dynamic displacements are applied using a piezoelectric actuator and the crystal is compressed mechanically (see Methods). Two configurations are studied: one with the actuator on the right ('reverse configuration', Fig. 1a), and the other with the actuator on the left ('forward configuration', Fig. 1b). The dynamic force–time history of the propagating waves is measured with *in situ* piezoelectric sensors[5]. In both configurations, one sensor is placed four sites away from the actuator and the other is placed at the other end. See Supplementary Information for more details on the experimental configuration.

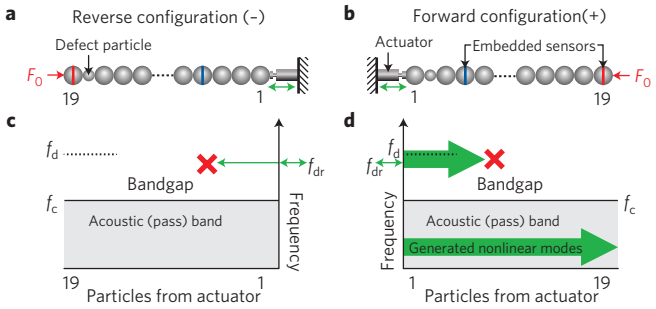

Figure 1 | Schematics and conceptual diagrams. a,**b**, Schematics of the granular crystal used in the experiments, composed of 19 stainless steel spherical particles, a light mass defect and applied static load F_0. Vertical lines in the spheres indicate the sensor particles. **c**,**d**, Conceptual diagrams of the rectification mechanism. f_d is the defect frequency, f_c is the acoustic (pass) band cutoff frequency and f_{dr} is the driving frequency. **a**,**c**, Reverse configuration: driving far from the defect, the bandgap filters out vibrations at frequencies in the gap. **b**,**d**, Forward configuration: driving near the defect, nonlinear modes are generated that transmit through the system.

A statically compressed homogeneous granular crystal acts as a low-pass frequency filter[24–26]. When the particles are identical, the crystal supports one band of propagating frequencies, called the acoustic band, extending from frequency $f = 0$ to the upper cutoff frequency f_c. Vibrations with frequencies $f > f_c$ lie in a bandgap and cannot propagate through the crystal[11]. The presence of a light mass defect breaks the periodicity of the crystal and induces an exponentially localized mode with frequency $f_d > f_c$ (refs 27, 28). Frequencies f_c and f_d depend on the geometric and material properties of the system and are proportionally tunable by the static load (see Methods and Supplementary Information; refs 24–28). The experimental characterization of the linear spectra can be seen in Supplementary Fig. S1.

A schematic of our rectifier concept is shown in Fig. 1c,d. We drive one end of the crystal harmonically. We fix the frequency of the driver f_{dr} at a frequency in the gap, below f_d, and increase the driving amplitude δ. As a result of the bandgap, in the reverse direction, the energy provided by the actuator does not propagate through the crystal. In the forward configuration, for low driving amplitudes, the actuator excites a periodic (at

Engineering and Applied Science, California Institute of Technology, Pasadena, California 91125, USA. †These authors contributed equally to this work.
*e-mail: daraio@caltech.edu.

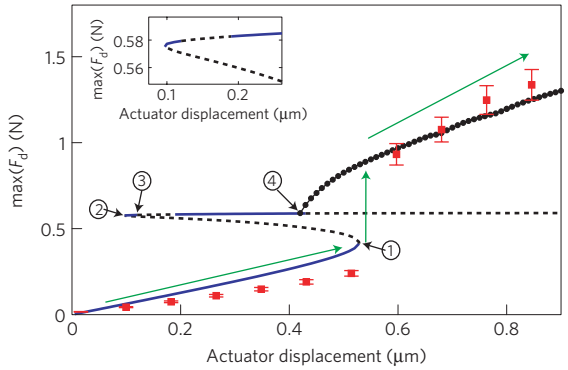

Figure 2 | Bifurcation and stability. Maximum dynamic force at the fourth particle from the actuator in the forward configuration as a function of driving amplitude δ (the actuator displacement). Red square markers are experimental data corresponding to the ($f_{dr} = 10.5$ kHz, $F_0 = 8$ N) configuration shown in Figs 1b and 3. Error bars are based on the range of actuator calibration values. The solid blue (dashed black) line corresponds to the numerically calculated stable (unstable) periodic branches. The dotted black line corresponds to the numerically calculated quasiperiodic branch. Green arrows denote the path (and jump) followed with increasing driving amplitude. The circled numbers correspond to bifurcation points. The inset shows the region around points 2 and 3 in greater detail.

frequency f_{dr}) vibrational mode localized around the defect. In this case, the energy does not propagate through the crystal. As the amplitude of the driver is increased, the system jumps from this low-amplitude stable periodic solution to a high-amplitude stable two-frequency quasiperiodic mode: one frequency being f_{dr} and the other being f_N. In our nonlinear system, this results in the distribution of energy to frequencies that are linear combinations of these two frequencies, including energy at low frequencies within the propagating band. A further increase of the driving amplitude induces chaotic vibrations, where the energy is redistributed along broad frequency bands surrounding the peaks of the quasiperiodic state. In both quasiperiodic and chaotic states the energy at low frequencies is transmitted.

To understand the transition between states occurring in the forward configuration of our system, we conduct parametric continuation using the Newton–Raphson (NR) method in phase space[26] and numerical integration of equation (1) (see Methods and Supplementary Information). To account for the dissipation in our system, we use linear damping (a damping coefficient $\tau = 1.75$ ms is selected to match experimental results). The actuator boundary is modelled as a moving wall, and the opposite boundary as a free boundary with an applied force. Applying the NR method, we follow the periodic family of solutions as a function of driving amplitude δ and study its linear stability. Figure 2 shows the maximum dynamic force amplitude (four particles away from the actuator) for each solution as a function of the driving amplitude for the granular crystal of Fig. 1 (with $F_0 = 8$ N, $f_{dr} = 10.5$ kHz, $\Delta f = f_d - f_{dr} \approx 500$ Hz, $f_c = 6.9$ kHz). The stable (unstable) periodic solutions are denoted by solid blue (dashed black) lines. At turning points 1 and 2, stable and unstable periodic solutions collide and mutually annihilate (saddle-centre bifurcation[14]). At points 3 and 4, the periodic solution changes stability and a new two-frequency stable quasiperiodic state emerges. As a result of the demonstrated bifurcation picture, we predict, with increasing amplitude, a progression of the system response following the low-amplitude stable periodic solution up to point 1, where the system jumps past the unstable periodic solution to the high-amplitude stable quasiperiodic state.

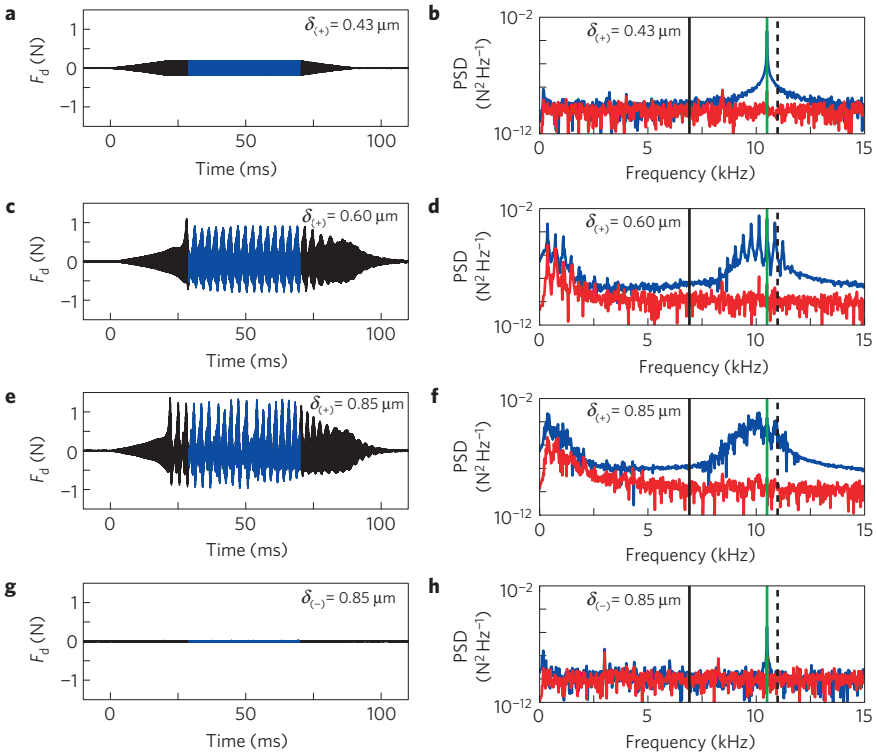

Figure 3 | Experimental force–time response and power spectra. a–f, Forward configuration. **g**,**h**, Reverse configuration. **a**,**c**,**e**,**g**, Experimentally measured force–time history for the sensor four particles away from the actuator ($f_{dr} = 10.5$ kHz, varying amplitude δ in the forward configuration). The blue is the time region used to calculate the PSDs. **b**,**d**,**f**,**h**, PSD of the measured force–time history for the sensors four (blue) and 19 particles away from the actuator (red). The vertical black solid line is the upper acoustic band cutoff frequency f_c, the black dashed line the defect mode frequency f_d, and the green line the driving frequency f_{dr}.

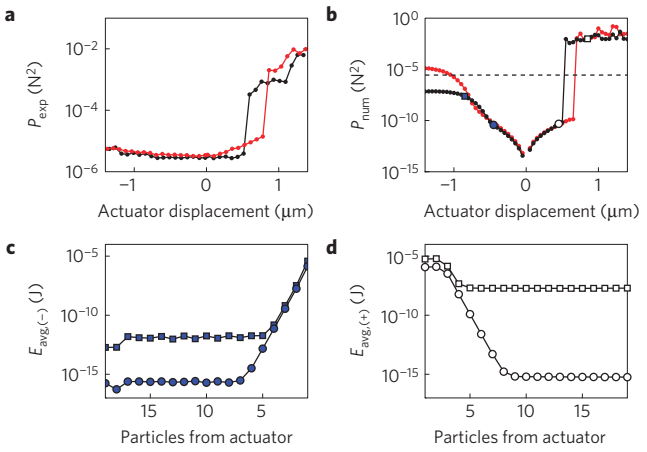

Figure 4 | Power transmission and energy distribution. a,**b**, Experimental (**a**) and numerical (**b**) average transmitted power as a function of driving amplitude δ (actuator displacement). The black curve corresponds to $F_0 = 8$ N ($f_{dr} = 10.5$ kHz) and the red (light grey) curve to $F_0 = 13.9$ N ($f_{dr} = 11.4$ kHz). Positive/negative displacements denote forward/reverse configurations, respectively. The horizontal black dashed line in **b** is the experimental noise floor. **c**,**d**, Numerical time-averaged energy density as a function of position for the reverse (**c**) and forward (**d**) configurations. Each curve corresponds to the configuration/amplitude of the same marker type as in **b**.

To demonstrate this jump, we harmonically drive the granular crystal of Fig. 1 at frequency $f_{dr} = 10.5$ kHz (with $\Delta f = f_d - f_{dr} \approx 500$ Hz, $f_c = 6.9$ kHz, $F_0 = 8$ N). The driving amplitude is set to δ for 90 ms, except for the first and last 20 ms where the driving amplitude is linearly increased and decreased, respectively. The linear ramp allows us to follow the low-amplitude stable periodic state (see Fig. 2). The maximum dynamic force measured by the sensors is plotted as the red square markers in Fig. 2. Figure 3 demonstrates each of the states. The dynamic force F_d experimentally measured by the sensor four particles away from the actuator is shown in the left panels. The subscript of the driving amplitude δ denotes the direction, where (+) and (−) are the forward and reverse configurations, respectively. The power spectral densities (PSDs) of the highlighted time region are calculated for both sensors (right panels of Fig. 3). Each curve corresponds to the sensor of the same colour and configuration as in Fig. 1a,b. In the forward configuration, at low driving amplitude ($\delta_{(+)} = 0.43$ μm, Fig. 3a,b), a periodic response is observed, with no energy propagating above the noise floor. At higher driving amplitudes ($\delta_{(+)} = 0.60$ μm, Fig. 3c,d), a quasiperiodic response is observed, with the generation of a second frequency $f_N = 10.13$ kHz and linear combinations of f_N and f_d. The combinations within the passband are transmitted. Increasing the amplitude further ($\delta_{(+)} = 0.85$ μm, Fig. 3e,f), a chaotic response is seen, where the area between the frequencies in Fig. 3d is filled in. By reversing the crystal, even at high amplitudes ($\delta_{(-)} = 0.85$ μm, Fig. 3g,h) no transmission is observed, which illustrates the rectification effect. In numerical simulations we observe a similar behaviour within a band of driving frequencies below f_d. For the configuration of Figs 1 and 2 the band of frequencies is approximately 800 Hz wide.

To demonstrate the rectifier tunability with static load, we measure the average transmitted signal power P_{exp} (area under the PSD curves from 0 to 20 kHz) as a function of actuator displacement (Fig. 4a) for two different static loads (and driving frequencies). The black curve corresponds to the configurations in Figs 2 and 3, and the red curve is for a static load of $F_0 = 13.9$ N ($f_{dr} = 11.4$ kHz, $\Delta f \approx 550$ Hz). For these two configurations the power transmitted is at maximum ∼1.7% of the input power. Changing the static load causes f_d to change (see Methods), which allows the rectifier to operate within a wide range of driving frequencies. In both cases an asymmetric (with respect to directional configuration) energy transmission is observed, with a sharp transition between periodic and quasiperiodic/chaotic states.

Numerical integration of equation (1) shows the same qualitative response as in the experiments (see Fig. 4b and Supplementary Figs S2 and S3). In Fig. 4b we plot the numerically calculated average transmitted power P_{num} for the same configurations (corresponding to the same colours) as in Fig. 4a. Below the experimental noise floor, in the reverse configuration, the increasing transmission corresponds to $f_s = f_{dr}/2$ subharmonic generation. This phenomenon is generally present at high amplitudes in nonlinear systems and will result in transmission at sufficiently high driving amplitudes in the reverse configuration (although it could be avoided by using a sufficiently small defect with subharmonic frequency in the gap). To calculate the energy rectification ratio, we plot the time-averaged energy density (per particle site) as a function of particle number, for the reverse ($E_{avg,(-)}$, Fig. 4c) and forward ($E_{avg,(+)}$, Fig. 4d) configurations. Each curve in Fig. 4c,d corresponds to the numerical run in Fig. 4b of the same marker type. As shown by the square markers in Fig. 4c and d, for high amplitudes, the system decays exponentially down to the level of the propagating mode. In both directions (Fig. 4c,d), at low driving amplitude, the system decays exponentially down to the numerical noise floor. In this case, the maximum rectification ratio $\sigma = E_{avg(+)}/E_{avg(-)}$ for the particle furthest from the actuator is $\sigma \approx 10^4$, whereas, because of dissipation and conversion efficiency, the transmitted time-averaged energy density of the last particle is ∼0.35% of the first particle. We also show in Supplementary Fig. S4 how such rectifiers can be configured as AND and OR logic gates, and how the design could be scaled to operate at ultrasonic frequencies for biomedical applications.

By operating close to the bifurcation point, small perturbations can cause the system's response to switch from the low-amplitude non-transmitting state to the high-amplitude transmitting state, making it useful for sensing applications. The demonstrated frequency downshifting could also be useful in energy harvesting technologies with frequency-dependent absorptivity and emissivity. The flexibility of the system is enhanced because the operational frequencies are tunable by variation of the static load and by the geometric and material properties. This proposed method of tunable bifurcation-based mechanical rectification offers new ways to control the flow of energy.

Methods

Experimental setup. The stainless steel particles (316 type, with elastic modulus $E = 193$ GPa and Poisson's ratio $\nu = 0.3$; ref. 26) are positioned on two aligned polycarbonate rods. The defect particle is aligned with the axis of the crystal using a polycarbonate ring. We mount the piezoelectric actuator on a steel cube and place a soft spring ($K_S = 1.24$ kN m^{-2}) at the other end. The spring and crystal are compressed by positioning a second steel cube with respect to the first. The static load is measured by a load cell placed between the spring and the steel cube. The displacement of the actuator and embedded strain gauge are calibrated optically. We use sensors consisting of piezoelectric disks embedded between two halves of a spherical particle, constructed so as to preserve the bulk material properties of the sphere[5]. The output of our sensors is conditioned by voltage amplifiers and analog 30 kHz, eighth-order Butterworth low-pass filters. The conditioned sensor output is digitally filtered by means of 300 Hz, fifth-order Butterworth high-pass filters to remove 60 Hz electrical noise.

Model. We model our system as a chain of nonlinear oscillators[21]:

$$m_n \ddot{u}_n = A_n[\Delta_n + u_{n-1} - u_n]_+^{3/2} - A_{n+1}[\Delta_{n+1} + u_n - u_{n+1}]_+^{3/2} - \frac{m_n}{\tau}\dot{u}_n \qquad (1)$$

where $[Y]_+$ denotes the positive part of Y, u_n is the displacement of the nth sphere around the static equilibrium, m_n is the mass of the nth particle, and $\Delta_n = (F_0/A_n)^{2/3}$ is the static overlap. The contact coefficients $A_n = (2E/3(1-\nu^2))(R_{n-1}R_n/(R_{n-1}+R_n))^{1/2}$ are defined by the Hertz law potential between adjacent spheres, where R_n is the radius of the nth particle[20,21].

We linearize the conservative ($\tau = \infty$) equation (1) about the crystal's equilibrium state[24]. The homogenous crystal contains one band of propagating frequencies extending from $f = 0$ to $f_c = 1/2\pi\sqrt{4K_{RR}/M}$, where $K_{RR} = (3/2)A_{RR}{}^{2/3}F_0{}^{1/3}$ and A_{RR} is the contact coefficient between two large particles. We calculate the frequency of the defect mode[28] by considering a reduced three-particle eigensystem, where

$$f_d = \frac{1}{2\pi}\sqrt{\frac{2K_{Rr}M + K_{RR}m + K_{Rr}m + \sqrt{-8K_{Rr}K_{RR}mM + (2K_{Rr}M + [K_{RR} + K_{Rr}]m)^2}}{2mM}}$$

and $K_{Rr} = (3/2)A_{Rr}{}^{2/3}F_0{}^{1/3}$, where A_{Rr} is the contact coefficient between a large particle and the defect particle.

Received 12 April 2011; accepted 15 June 2011; published online 24 July 2011

References

1. Li, B., Wang, L. & Casati, G. Thermal diode: Rectification of heat flux. *Phys. Rev. Lett.* **93,** 184301 (2004).
2. Li, B. & Wang, L. Phononics gets hot. *Phys. World* **21,** 27–29 (March, 2008).
3. Chang, C. W., Okawa, D., Majumdar, A. & Zettl, A. Solid-state thermal rectifier. *Science* **314,** 1121–1124 (2006).
4. Kobayashi, W., Teraoka, Y. & Terasaki, I. An oxide thermal rectifier. *Appl. Phys. Lett.* **95,** 171905 (2009).
5. Nesterenko, V. F., Daraio, C., Herbold, E. B. & Jin, S. Anomalous wave reflection at the interface of two strongly nonlinear granular media. *Phys. Rev. Lett.* **95,** 158702 (2005).
6. Liang, B., Yuan, B. & Cheng, J. C. Acoustic diode: Rectification of acoustic energy flux in one-dimensional systems. *Phys. Rev. Lett.* **103,** 104301 (2009).
7. Liang, B., Guo, X. S., Tu, J., Zhang, D. & Cheng, J. C. An acoustic rectifier. *Nature Mater.* **9,** 989–992 (2010).
8. Li, X. F. *et al.* Tunable unidirectional sound propagation through a sonic-crystal-based acoustic diode. *Phys. Rev. Lett.* **106,** 084301 (2011).
9. Wang, L. & Li, B. Thermal logic gates: Computation with phonons. *Phys. Rev. Lett.* **99,** 177208 (2007).
10. Markos, P. & Soukoulis, C. M. *Wave Propagation: From Electrons to Photonic Crystals and Left-handed Materials* (Princeton Univ. Press, 2008).
11. Brillouin, L. *Wave Propagation in Periodic Structures* (Dover, 1953).
12. Sigalas, M. *et al.* Classical vibrational modes in phononic lattices: Theory and experiment. *Z. Kristallogr.* **220,** 765–809 (2005).
13. Eichenfield, M., Chan, J., Camacho, R. M., Vahala, K. J. & Painter, O. Optomechanical crystals. *Nature* **462,** 78–82 (2009).
14. Strogatz, S. H. *Nonlinear Dynamics and Chaos* (Perseus Publishing, 1994).
15. Maniadis, P., Kopidakis, G. & Aubry, S. Energy dissipation threshold and self-induced transparency in systems with discrete breathers. *Physica D* **216,** 121–135 (2006).
16. Karabalin, R. B. *et al.* Signal amplification by sensitive control of bifurcationtopology. *Phys. Rev. Lett.* **106,** 094102 (2011).
17. Vijay, R., Devoret, M. H. & Siddiqi, I. Invited review article: The Josephson bifurcation amplifier. *Rev. Sci. Instrum.* **80,** 111101 (2009).
18. Campbell, D. K., Flach, S. & Kivshar, Y. S. Localizing energy through nonlinearity and discreteness. *Phys. Today* **57,** 43–49 (January, 2004).
19. Soljačić, M. & Joannopoulos, J. D. Enhancement of nonlinear effects using photonic crystals. *Nature Mater.* **3,** 211–219 (2004).
20. Johnson, K. L. *Contact Mechanics* (Cambridge Univ. Press, 1985).
21. Nesterenko, V. F. *Dynamics of Heterogeneous Materials* (Springer, 2001).
22. Daraio, C., Nesterenko, V. F., Herbold, E. & Jin, S. Tunability of solitary wave properties in one dimensional strongly nonlinear phononic crystals. *Phys. Rev. E* **73,** 026610 (2006).
23. Coste, C., Falcon, E. & Fauve, S. Solitary waves in a chain of beads under Hertz contact. *Phys. Rev. E* **56,** 6104–6117 (1997).
24. Herbold, E. B., Kim, J., Nesterenko, V. F., Wang, S. Y. & Daraio, C. Tunable frequency band-gap and pulse propagation in a strongly nonlinear diatomic chain. *Acta Mech.* **205,** 85–103 (2009).
25. Hladky-Hennion, A. C. & de Billy, M. Experimental validation of band gaps and localization in a one-dimensional diatomic phononic crystal. *J. Acoust. Soc. Am.* **122,** 2594–2600 (2007).
26. Boechler, N., Theocharis, G., Job, S., Kevrekidis, P. G., Porter, M. A. & Daraio, C. Discrete breathers in one-dimensional diatomic granular crystals. *Phys. Rev. Lett.* **104,** 244302 (2010).
27. Job, S., Santibanez, F., Tapia, F. & Melo, F. Wave localization in strongly nonlinear Hertzian chains with mass defect. *Phys. Rev. E* **80,** 025602 (2009).
28. Boechler, N., Theocharis, G., Man, Y., Kevrekidis, P. G. & Daraio, C. Defect modes in one-dimensional granular crystals. Preprint at http://arxiv.org/abs/1103.2483 (2011).
29. Spadoni, A. & Daraio, C. Generation and control of sound bullets with a nonlinear acoustic lens. *Proc. Natl Acad. Sci. USA* **107,** 7230–7234 (2010).
30. Hong, J. Universal power-law decay of the impulse energy in granular protectors. *Phys. Rev. Lett.* **94,** 108001 (2005).

Acknowledgements

We thank M. C. Cross, C. Hannemann, P. G. Kevrekidis, M. A. Porter, A. W. Richards and T. Schneider for useful discussions. We thank V. Gabuchian, M. Mello and S. Job for help in the experiments. We acknowledge support from the National Science Foundation grants number 844540 (CAREER), 969541 and 0520565 (MRSEC). C.D. acknowledges the Office of Naval Research (YIP), and G.T. the A.S. Onassis Public Benefit Foundation through Grant No. RZG 003/2010-2011.

Author contributions

N.B. and G.T. developed the system concept. N.B. led the experimental work. G.T. led the theoretical and numerical analysis. C.D. provided guidance and contributed to the design and analysis throughout the project. All authors contributed to the writing and editing of the manuscript.

Additional information

The authors declare no competing financial interests. Supplementary information accompanies this paper on www.nature.com/naturematerials. Reprints and permissions information is available online at http://www.nature.com/reprints. Correspondence and requests for materials should be addressed to C.D.